Analysis of magnetic field plasma interactions using microparticles as probes

Michael Dropmann,[1,2,*] Rene Laufer,[1,2] Georg Herdrich,[1,2] Lorin S. Matthews,[1] and Truell W. Hyde[1,†]

[1]*Baylor University, Center for Astrophysics, Space Physics and Engineering Research (CASPER), One Bear Place 97310, Waco, Texas 76798-7310, USA*

[2]*Institute of Space Systems, University of Stuttgart, Raumfahrtzentrum Baden-Wuerttemberg, Pfaffenwaldring 29, 70569 Stuttgart, Germany*

(Received 16 March 2015; published 26 August 2015)

The interaction between a magnetic field and plasma close to a nonconductive surface is of interest for both science and technology. In space, crustal magnetic fields on celestial bodies without atmosphere can interact with the solar wind. In advanced technologies such as those used in fusion or spaceflight, magnetic fields can be used to either control a plasma or protect surfaces exposed to the high heat loads produced by plasma. In this paper, a method will be discussed for investigating magnetic field plasma interactions close to a nonconductive surface inside a Gaseous Electronics Conference reference cell employing dust particles as probes. To accomplish this, a magnet covered by a glass plate was exposed to a low power argon plasma. The magnetic field was strong enough to magnetize the electrons, while not directly impacting the dynamics of the ions or the dust particles used for diagnostics. In order to investigate the interaction of the plasma with the magnetic field and the nonconductive surface, micron-sized dust particles were introduced into the plasma and their trajectories were recorded with a high-speed camera. Based on the resulting particle trajectories, the accelerations of the dust particles were determined and acceleration maps over the field of view were generated which are representative of the forces acting on the particles. The results show that the magnetic field is responsible for the development of strong electric fields in the plasma, in both horizontal and vertical directions, leading to complex motion of the dust particles.

DOI: 10.1103/PhysRevE.92.023107 PACS number(s): 52.25.Xz, 52.27.Lw, 52.40.Kh, 94.05.Bf

I. INTRODUCTION

The interaction between plasma and magnetic fields is of great interest across many areas of research. Space plasmas, such as the solar wind, interact both with stellar and planetary magnetic fields. These fields can globally enclose a celestial body, as is the case for many planets, or occur as localized patches, as seen on smaller bodies without an active core dynamo, for example the Moon. In the latter case, complex interactions can occur between the magnetic field, the plasma, and the Moon's surface, significantly affecting processes taking place at the surface. For example, dust transport and space weathering on the Moon have been proposed as possible sources for the formation of the bright albedo patterns on the lunar surface called lunar swirls [1]. The physics behind the plasma magnetic field interaction theorized to create this effect is currently under investigation in various laboratory experiments [2–4]. Plasma interactions with magnetic fields also play an important role in many technologies currently under development. For example, magnetic confinement is used to control the extremely hot plasma in some fusion experiments and protect the plasma facing components [5]. Future space technology applications will also make use of magnetic fields in various ways. For example, in space propulsion, magnetic fields may be used as a nozzle for electric propulsion systems [6], a collector for the interstellar medium to operate a fusion reactor during interplanetary and interstellar travel [7], or as a solar sail in the case of mini-magnetospheric plasma propulsion [8]. The ability to deflect plasma with magnetic fields may also be of use as a protective shield from cosmic radiation [9] or for heat flux reduction during the atmospheric entry of spacecraft [10]. In each of these, a proper understanding of the physics behind the interaction between the plasma and local or global magnetic fields is essential.

The experiments discussed in this paper are designed to provide a better understanding of the interaction between the lunar plasma environment, primarily fed by the solar wind, and magnetic anomalies on the Moon and explore their relevance for the formation of lunar swirls.

Specifically, a method using micron-sized dust particles as probes for analyzing the interaction between the plasma and the magnetic field will be presented. The data produced by this method allows the generation of two-dimensional acceleration maps for particles in a plasma perturbed by a magnetic field. The results provide data concerning the resulting electric fields in the plasma and thus the interaction of the plasma with the magnetic field.

The paper is presented in the following manner. In Sec. II the experimental setup is described, in Sec. III the data analysis method is developed, and Sec. IV presents the results, which are then discussed in Sec. V. Finally conclusions are provided in Sec. VI.

II. EXPERIMENTAL SETUP

The experiments discussed here were conducted in a modified Gaseous Electronics Conference reference cell, which is a standardized capacitively driven rf-plasma cell [11]. The electrodes have diameters of 100 mm with an interelectrode spacing of 19 mm. The lower electrode is powered at 13.56 MHz while the upper electrode and chamber act as ground. The upper electrode is ring shaped, allowing optical access from the top of the cell and the ability to introduce particles of micrometer size into the experiment.

*michael_dropmann@baylor.edu
†truell_hyde@baylor.edu

 ©2015 American Physical Society

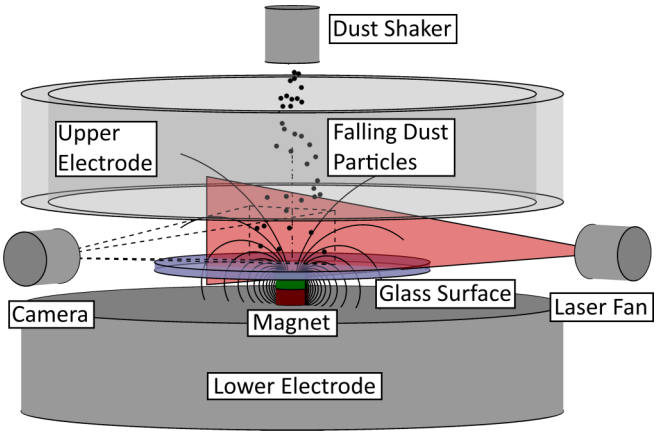

FIG. 1. (Color online) Schematic of the experimental setup. The magnet is placed on the lower electrode and covered by a glass plate. Dust is dropped from above the upper electrode into the plasma and illuminated by a fanned diode laser. A high-speed camera perpendicular to the laser plane records the dust particle trajectories.

A cylindrical NdFeB magnet, 6.35 mm in both length and diameter, was placed on the lower electrode beneath a glass plate of 1.5 mm thickness and 50.8 mm diameter. Glass was chosen to ensure that the surface remains nonconductive and avoid unwanted surface currents. The magnet was of grade 40 SH with a magnetic remanence of 1.24−1.28 T. The glass is centered using a Teflon [polytetrafluoroethylene] structure, which also holds the magnet. The magnet is separated from the lower electrode with a Teflon spacer of 1 mm thickness. A schematic view of the experimental setup is shown in Fig. 1. The magnetic field lines and intensity within the experimental setup have been determined numerically with FEMM [12] and are plotted to scale in Fig. 2. For all experiments described here, the pressure was held at 5.3 Pa and the system was held at a peak-to-peak voltage of 84 V producing a plasma of 11 W. In previous experiments conducted at CASPER [13], Langmuir probe measurements in the plasma bulk have been collected at pressures down to 8.6 Pa. Extrapolation of that data indicates an electron temperature of 5 eV and a plasma density of 2×10^{15} m^{-3} for the given conditions. Within the plasma bulk, ions are assumed to be in thermal equilibrium with the neutrals and thus at room temperature. In the sheath, however, which has a thickness of 5 mm or more, as shown later, strong

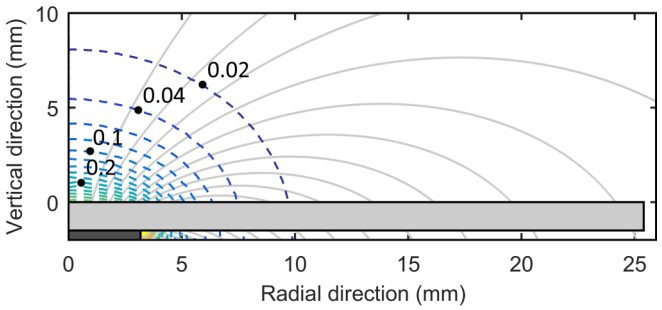

FIG. 2. (Color online) Magnetic field lines for the experimental setup discussed. The left side of the plot represents the symmetry axis. The magnetic flux density is plotted with dashed lines representing lines of constant field in increments of 0.02 T. Solid lines represent the magnetic field lines themselves.

electric fields are present. The measured bias of the lower electrode is −85 V. This leads to an electric field in the sheath having a magnitude of 10 kV/m. This field accelerates the ions towards the lower electrode. However, the speed of the ions is limited by collisions with neutrals and can be calculated as [14]

$$v_i = \sqrt{\frac{qE}{m_i n_n \sigma}}. \quad (1)$$

In the above, q is the ion charge, E is the electric field strength, m_i is the ion mass, n_n is the neutral density, and σ is the collision cross section. The collision cross section for an Ar^+-Ar collision is 1×10^{-18} m^2 [15]. The neutral density at the given pressure and room temperature is 1.28×10^{21} m^{-3}. Based on Eq. (1), ions will move with an average speed of approximately 4 km/s in the sheath, equivalent to an energy of 4 eV.

Microparticles consisting of 12 μm-diameter melamine formaldehyde (MF) spheres with a density of 1.51 g cm^{-3}, as provided by the manufacturer, are used for diagnostic purposes in this experiment. A diode laser mounted outside the chamber was fanned vertically to illuminate the dust particles. A Photron 1024 charge-coupled device high-speed camera with a field of view of approximately 10 mm in the vertical direction and 20 mm in the horizontal direction at the laser plane was oriented perpendicularly to the laser plane to allow imaging of the particles at a frame rate of 2000 fps. By moving the camera in the horizontal direction and combining subsequent datasets, particle trajectories were mapped over an area measuring 10 mm by 50 mm. During each experimental run, several hundred microparticles were dropped into the plasma using the dust dispenser. Particle trajectories within the laser-illuminated plane were recorded using the high-speed camera for later analysis.

The dust particle charge must be known in order to derive the electric field strength from the electric force acting on the particles. Past measurements indicate that the charge is on the order of several 1×10^4 elementary charges [16]; however, as the magnetic field may have an impact on local electron temperatures and ion speeds, such values must be considered approximations for this experiment. Under the operating conditions used, magnetized electrons and unmagnetized ions, a decreased dust charge is expected [17]. Due to uncertainties in the particle charge, these values will only be used to determine the order of magnitude of the electric field strength.

For each experiment, a reference experiment without a magnet was also conducted in order to verify the effect of the magnet on the system.

Based on these parameters, the Larmor radii for both electrons and ions can be calculated using [14]

$$r_g = \frac{m v_\perp}{|q|B}. \quad (2)$$

Table I lists the Larmor radii at multiple positions in the experiment.

For comparison, the mean free path of Ar^+ and electrons can be calculated using [14]

$$\lambda = \frac{1}{\sqrt{2}\sigma n_n}. \quad (3)$$

TABLE I. Larmor radii for electrons and ions.

Vertical position (mm)	Radial position (mm)	Flux density (T)	Electron Larmor radius (mm)	Ion Larmor radius (mm)
0	0	0.3	0.018	6
0	7	0.04	0.133	45
6	0	0.04	0.133	45
0	25.4	0.0012	4.4	1500

Note that only collisions with neutrals are considered given that the degree of ionization is on the order of 1×10^{-6}. Using the collision cross sections 1×10^{-18} m^2 for Ar^+-Ar [15] and 7.6×10^{-20} m^2 for e-Ar [18], the resulting mean free paths are 0.5 mm for Ar^+ and 7.3 mm for electrons. This indicates that the magnetic field can be neglected for ion motion, since the Larmor radii are at least one order of magnitude larger than the mean free path and substantially larger than the thickness of the plasma sheath. For electrons the situation is different. The Larmor radius is two orders of magnitude smaller than the mean free path at the center of the plate and half the mean free path at the outer edge of the plate. Thus the magnetization of electrons is significant in the region where data was collected.

III. DATA ANALYSIS

Data collected by the high-speed camera were preprocessed by subtracting the background and adjusting the contrast and brightness of the pictures to reduce background noise and enhance overall visibility of the particles. A MATLAB-based algorithm for particle detection was employed to identify the particles in each frame which were then linked using the Hungarian algorithm [19].

The resulting data were translated into a standard coordinate system, the trajectories smoothed, and particle velocities and accelerations calculated, based on the first and second order difference quotient. Filtering eliminated faulty spots in the trajectories by identifying discontinuities in the calculated accelerations. Trajectories exhibiting minimal particle movement were also removed as these are usually associated with noise falsely interpreted as particles. This resulted in a dataset listing particle positions, velocities, and accelerations in both horizontal and vertical directions. These data were then used to generate accelerations maps.

A grid for the acceleration maps was defined which covered the range of recorded particle trajectories. For each grid point, the acceleration is calculated as the average acceleration of all data points within a radius $R = 1$ mm of the grid point. Representative particle trajectories and the circular area of radius R for data collection for one grid point are shown in Fig. 3.

A. Forces

Total acceleration of the microparticles is driven by gravity $\vec{F}_G$, the electric force $\vec{F}_E$, the magnetic force $\vec{F}_B$, the thermophoretic force $\vec{F}_T$, and the drag force. The drag force can be subdivided into two components: the neutral drag $\vec{F}_{n,\mathrm{drag}}$ and the ion drag $\vec{F}_{i,\mathrm{drag}}$. The resulting equation of motion for the particles is

$$m\ddot{\vec{r}} = \vec{F}_G + \vec{F}_E + \vec{F}_B + \vec{F}_T + \vec{F}_{n,\mathrm{drag}} + \vec{F}_{i,\mathrm{drag}}. \quad (4)$$

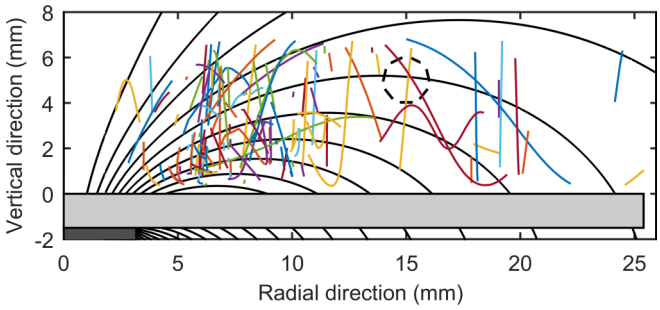

FIG. 3. (Color online) Representative experimentally measured particle trajectories. Only a small number of data points (1619 out of 84 727) are shown for clarity. The left side of the plot is the symmetry axis of the experiment. The light-gray box indicates the glass plate above the magnet, represented by the dark-gray box. The black lines in the background are the magnetic field lines and the dashed circle indicates the region used for the acceleration determination at this spot.

Both the mass of the particles and the gravitational acceleration are known, allowing the gravitational force to be subtracted from the other forces. In the following, the accelerations caused by the different force components are estimated to determine if the respective influence can be neglected or needs to be calculated more carefully. As the accelerations observed in the experiment are on the order of 0.1−5 g, forces significantly weaker than 0.1 g will be neglected.

1. Neutral drag force

The neutral gas background is assumed to have no macroscopic flow velocity. Thus, in the Epstein regime [20] the neutral drag force is linearly proportional to the particle velocity v at low speeds:

$$F_{\mathrm{Epstein}} = -\beta v, \quad (5)$$

where β is defined as

$$\beta = \delta \frac{4\pi}{3} a^2 N m_n \bar{c}_n. \quad (6)$$

In the equation above, a is the particle radius, N is the neutral gas number density, m_n is the neutral mass (of argon) and the coefficient δ accounts for the type of reflection or absorption of the neutral gas particle. For melamine formaldehyde particles in argon this coefficient was determined to be 1.44 [21,22]. Finally, the thermal speed $\bar{c}_n$ is defined as

$$\bar{c}_n = \sqrt{\frac{8kT}{\pi m}}. \quad (7)$$

Equation (6) yields a value of $\beta = 7.49 \times 10^{-12}$ N m^{-1} s. Based on this value and the measured particle velocities, the acceleration from the neutral drag force can be subtracted from the data.

The Epstein coefficient was also determined experimentally from the data for comparison. To accomplish this, velocities

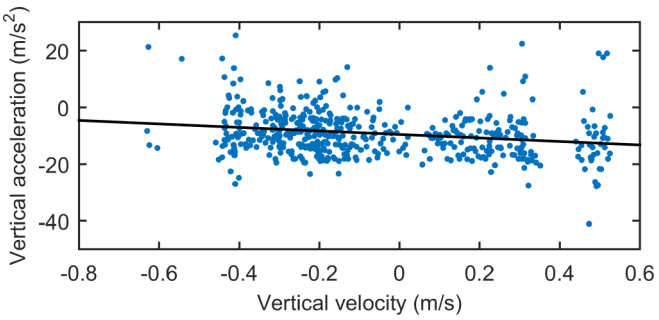

FIG. 4. (Color online) Radial velocity versus radial acceleration for all data points within the circle shown in Fig. 3. The dashed line shows the regression curve as described in the text.

and accelerations within a radius R at each grid point were used to generate a velocity versus acceleration plot (Fig. 4). As the neutral drag force is the only force that depends on the particle velocity, the slope of a linear regression curve fit to a velocity versus acceleration plot represents the quotient of the Epstein drag coefficient β and the particle mass. All other forces, being independent of particle velocity, simply shift this curve in the vertical direction and without changing the slope. By multiplying by the particle mass, the drag coefficient at each grid point can now be determined. Since this result is more accurate for higher particle velocities, only the vertical motion is considered for the determination of the drag coefficient. A histogram of the calculated drag coefficients is generated and fitted using a normal distribution function. For the case without a magnet, a drag coefficient of $7.81 \times 10^{-12}\,\mathrm{N\,m^{-1}\,s}$ with a standard deviation of $2.54 \times 10^{-12}\,\mathrm{N\,m^{-1}\,s}$ was determined. For the case with a magnet, the coefficient was determined to be $7.62 \times 10^{-12}\,\mathrm{N\,m^{-1}\,s}$ with a standard deviation of $2.72 \times 10^{-12}\,\mathrm{N\,m^{-1}\,s}$. These values are 4.3% and 1.8% higher than predicted and consequently in good agreement with the analytically calculated value from Eq. (6). In the data analysis the analytically calculated value has been used to compensate for this force.

2. Ion drag force

As the ions in the sheath have a high velocity directed towards the electrode, the plasma is highly anisotropic in the sheath and the ion drag force can be estimated using [23]

$$F_I = -\pi a^2 m_i n_i v_i^2. \tag{8}$$

Using the plasma bulk density to provide a conservative estimate, since decreased ion densities are expected in the sheath, the acceleration caused by the ion drag force is approximately 1.8×10^{-2} g. Thus the ion drag force may be considered negligible.

3. Thermophoretic force

Since no external thermal gradient is applied to the plasma, and the ion densities and thus the heating of the neutral gas are small, the thermophoretic force may be considered negligible [24].

4. Magnetic force

The acceleration caused by the magnetic force acting on the particles can be calculated using [14]

$$\vec{F}_B = q \cdot \vec{v} \times \vec{B}, \tag{9}$$

with q the charge of a dust particle, m the dust particle mass, $\vec{v}$ the particle velocity, and $\vec{B}$ the magnetic flux density. As a conservative overestimate, the charge will be on the order of 1×10^5 elementary charges and the maximum velocity on the order of 0.5 m/s. From calculations the maximum magnetic flux density in the region is 0.3 T at the surface. The accelerations caused by the magnetic forces will be smaller than 2×10^{-4} g and can be neglected.

5. Electric force

After eliminating all other forces, the remaining force largely represents the electric force acting on the particles and is itself a combination of the forces resulting from the electric fields in the plasma sheath and the interparticle interactions. To eliminate perturbations due to particle interactions, data from isolated particles (distance to nearest neighbor $\geqslant$ 2 mm) are used to generate the final acceleration map. Assuming conservatively 1×10^5 elementary charges per dust particle and an unscreened Coulomb interaction, at this distance the interparticle force is two orders of magnitude smaller than gravity and can be neglected.

IV. RESULTS

A. Acceleration maps

Acceleration maps for experiments with and without a magnetic field in both the radial and vertical directions are presented in Figs. 5 and 6, respectively. Note that both the neutral drag force and gravitational force have been removed from the data as described previously. As such, all plots provide an estimate of the acceleration due solely to the electric force.

Figure 5(a) shows the horizontal acceleration of the dust particles with no magnet present. A weak acceleration of approximately 0.15 g pointing away from the center of the glass plate can be observed up to a vertical distance of 4 mm above the glass plate. Above this no significant radial acceleration was detected in the experiment.

Figure 6(a) shows the vertical acceleration of the particles with no magnetic field present. The levitation height of the particles, defined as the height where their vertical acceleration is equal to 1 g, occurs at a maximum of 5.5 mm at the center of the plate and decreases almost linearly to 2 mm towards the edges of the glass plate. At the surface of the glass plate the magnitude of the vertical acceleration ranges from 2.5 g at the center to 2 g at the edges. The acceleration profile of the sheath is monotonic in the vertical direction.

Figure 5(b) shows the horizontal acceleration of the dust particles with the magnet in place. As shown, a strong repulsive force acts on the dust particles as they approach the cusp region of the magnet and is greatest near the surface of the glass. This repelling force has a maximum magnitude of 2 g and changes direction to a radially inward-directed force at a radial position of 6.5 mm. This change in direction leads to a particle confinement region in the horizontal direction at this

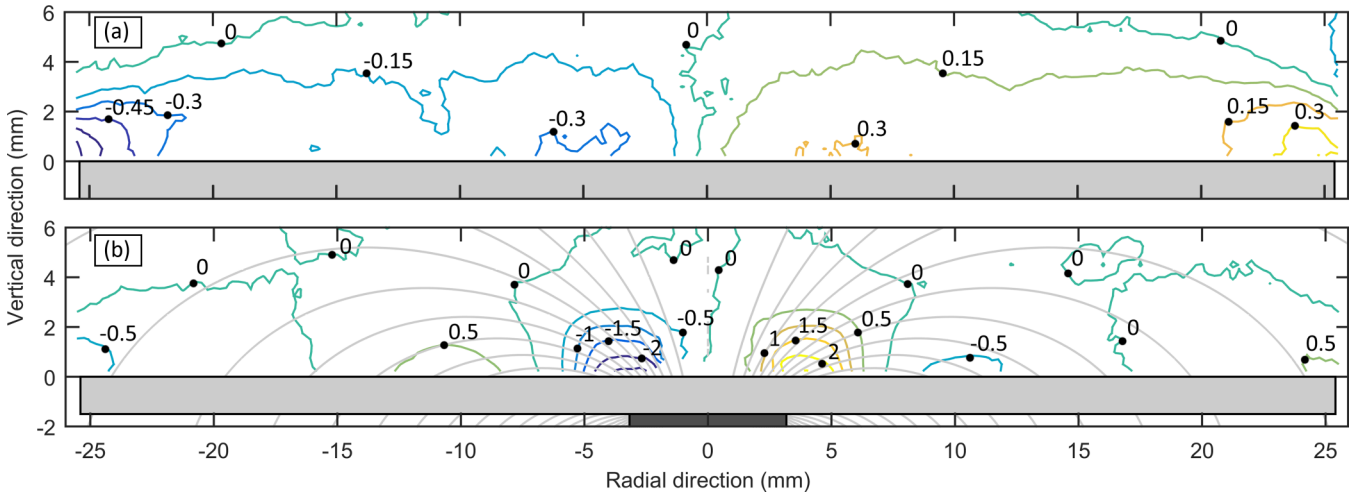

FIG. 5. (Color online) Contour plot of radial accelerations of 12 micron MF particles with (a) no magnetic field and (b) with magnetic field. The numbers on the contours represent the acceleration in units of g. The gray lines in (b) represent the magnetic field lines.

position. This inward-directed force has a maximum of 0.5 g, changing direction at a radial position of 15 mm to a radially outward directed force, before reaching a magnitude of 0.5 g. The influence of the magnetic field in the horizontal direction appears to vanish with increasing height and is not measurable at distances greater than 3 mm above the plate.

Figure 6(b) shows the vertical acceleration for the particles when a magnetic field is present. The thickness of the sheath region, here defined as the layer where the vertical acceleration is greater than zero, in general has a smaller vertical extent than in the case without a magnetic field, with the vertical acceleration strongest close to the surface. Over the regime examined, the vertical sheath profile and maximum acceleration at the surface change significantly in the radial direction. Immediately above the magnet the levitation height is approximately 4 mm. The levitation height dips to 2 mm at a radial position of 6.5 mm with a slight increase at larger radial distances. This minimum at a radial position of 6.5 mm corresponds to the position of horizontal confinement mentioned earlier and provides a confinement stability point in both the horizontal and vertical directions. Consequently stable dust levitation is observed here during the experiment.

B. Sheath profiles

The acceleration maps show that the sheath thickness is significantly changed by the addition of a magnetic field. This can be seen by examining the acceleration profiles in the vertical direction, plotted at three radial positions both with and without a magnet (see Fig. 7). At all positions the sheath profile resembles a bell curve with maximum acceleration closest to the surface and decreasing with increasing height. For the case without a magnet, the magnitude decreases only slightly with increasing radial displacement. For cases with the magnet, the acceleration closest to the surface is significantly greater at radial positions of 0 and 13 mm and decays faster in the vertical direction than in cases without a magnet. In contrast, at positions where the dust particles can be stably confined

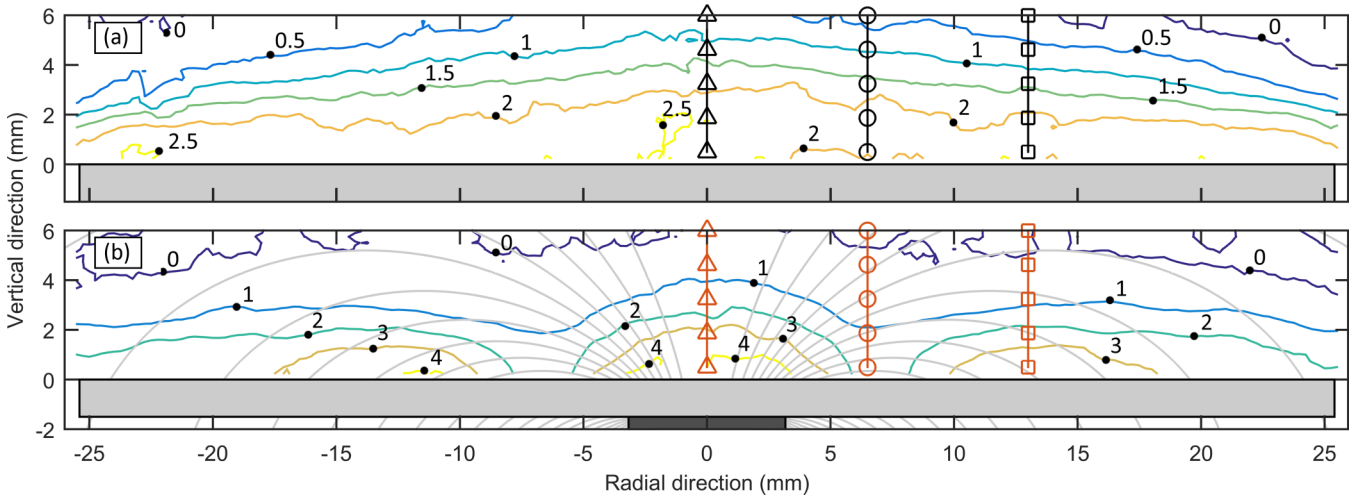

FIG. 6. (Color online) Contour plot of the vertical accelerations of 12 micron MF particles with (a) no magnetic field and (b) with magnetic field. The numbers on the contours represent the acceleration in units of g. The light-gray lines in the case with a magnetic field represent the field lines. Vertical lines mark the position of the sheath profiles in Fig. 7.

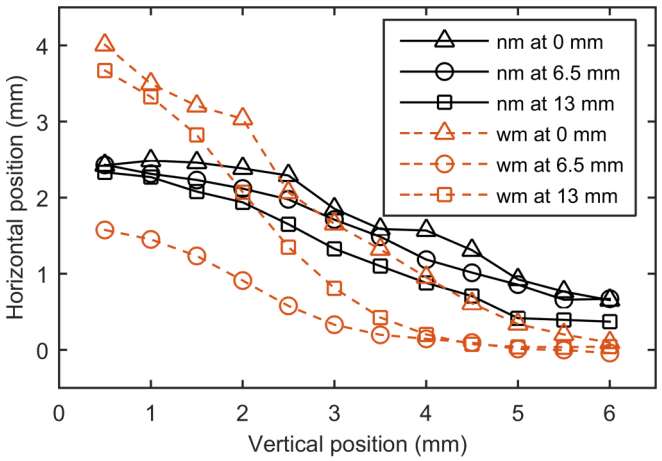

FIG. 7. (Color online) Vertical acceleration profiles at different radial positions with (wm) and without (nm) magnet. The positions of the sheath profiles are indicated in Fig. 6.

(radius 6.5 mm), the acceleration at the surface decreases when a magnet is present.

V. DISCUSSION

Due to the small ratio of Larmor radius to mean free path, the cross-field diffusion of electrons is strongly inhibited leading to an electron flow occurring preferentially along the magnetic field lines. This effect manifests as minimum points in the vertical electric field within the sheath, for example as seen in Fig. 6(b) at a radius of 6.5 mm. Here, the magnetic field is directed horizontally leading to an inhibited electron flux towards the surface. As a result the glass surface at this point charges less negatively than its surroundings, producing an overall weaker vertical electric field in this region. Electrons which are bound to these horizontal field lines will either travel to the center or outwards, where the field lines intersect the surface of the plate leading to a more negative potential at these locations. This can be confirmed by comparing the vertical accelerations of the microparticles without the magnet [Fig. 6(a)] and with the magnet [Fig. 6(b)]. The repulsive vertical acceleration from the surface increases from the center outwards and is surrounded by a region of decreasing acceleration which is itself surrounded by a region with increasing acceleration. At the edge of the table the sheath thickness appears similar for both the case with the magnet and without the magnet since the magnetic flux density is weakest in this region. These differences in surface charge for differing radii lead to significant forces in the horizontal direction as shown in Fig. 5(b).

Qualitatively, these results at the surface are comparable to emissive probe data gathered by Wang [2]. In this case, a negative surface potential in the cusp region was measured surrounded by a less negative region, where the field lines were horizontal, which was itself surrounded by a more negative region.

Note that not only surface charges are responsible for the described fields. The redistribution of electrons within the plasma volume itself by the magnetic field can lead to modified charge densities leading to strong electric fields and a change in particle charge. Here as well the magnetic mirror effect is of importance. Electrons that follow the field lines into the region where the magnetic field converges (the cusp region of the magnet) will encounter a Lorentz force component that will accelerate them towards the diverging direction of the magnetic field. Electrons moving at an angle greater than the maximum pitch angle θ_m, defined as [14]

$$\sin^2\theta_m = \frac{B_0}{B_m} \tag{10}$$

with B_0 the magnetic flux density at the electron position and B_m the maximum flux density at the surface, will then be reflected by the converging magnetic field before intersecting with the surface. This leads to a reduction in electron flux towards the surface in the cusp region and an increased electron flux at larger radial distances where the field lines intersect the plate surface.

The impact of the magnetic field on the electron density also modifies plasma parameters like the Debye length. An increase in electron density will lead to a decrease in the Debye length and consequently stronger electric field gradients in the sheath. This results in the decrease of the sheath thickness seen in Fig. 7.

VI. CONCLUSIONS

A method using micron-sized melamine formaldehyde particles as probes has been used to map the electric forces acting on these particles within a plasma and investigate the interaction of plasma with a nonconducting surface in the presence of a magnetic field. The effects due to the neutral drag and gravitational force have been isolated and removed from the data. Other contributions to the force acting on the particles have been shown to be negligible, leading to a good estimation of the acceleration due to the electric force and thus the electric field present in the sheath.

A comparison of acceleration maps generated with and without a magnetic field indicates that introducing a magnetic field to the system in the manner described strongly impacts the plasma sheath, particularly close to the surface of the glass plate. Since the magnetic field is not strong enough to significantly affect the plasma ions directly, the changes observed within the plasma sheath must primarily be caused by the interaction of plasma electrons with the magnetic field. The resulting modification of the electron density distribution in the plasma volume and the inhomogeneous surface potential caused by the changed electron fluxes produces strong horizontal electric fields. These fields significantly affect plasma ion trajectories, increasing the ion flux in certain regions and decreasing it in others, leaving portions of the surface of the glass plate "shielded" from the ion flux.

Thus, the interaction of plasma electrons with a magnetic field can generate regions of changed electron density, creating strong electric fields that can alter the ion flow to a much greater extent than the pure interaction of these ions with the magnetic field alone would allow.

ACKNOWLEDGMENTS

This work was supported by the National Science Foundation under Grants No. 1262031 and No. 1414523.

[1] L. L. Hood and C. R. Williams, in *Proceedings of the 19th Lunar and Planetary Science Conference, 1989* (Cambridge University Press/Lunar and Planetary Institute, Cambridge, 1989), pp. 99–113.
[2] X. Wang, C. T. Howes, M. Horányi, and S. Robertson, Geophys. Res. Lett. **40**, 1686 (2013).
[3] X. Wang, M. Horányi, and S. Robertson, J. Geophys. Res. Space Phys. **117**, A06226 (2012).
[4] R. A. Bamford, B. Kellett, W. J. Bradford, C. Norberg, A. Thornton, K. J. Gibson, I. A. Crawford, L. Silva, L. Gargaté, and R. Bingham, Phys. Rev. Lett. **109**, 081101 (2012).
[5] W. M. Stacey, *Fusion: An Introduction to the Physics and Technology of Magnetic Confinement Fusion* (Wiley, New York, 2010).
[6] A. V. Arefiev and B. N. Breizman, Phys. Plasmas 1994–Present **11**, 2942 (2004).
[7] R. W. Bussard, Astronautica Acta **6**, 179 (1960).
[8] G. Herdrich, U. Bauder, A. Boxberger, R. A. Gabrielli, M. Lau, D. Petkow, M. Pfeiffer, C. Syring, and S. Fasoulas, Vacuum **88**, 36 (2013).
[9] R. Bamford, K. J. Gibson, A. J. Thornton, J. Bradford, R. Bingham, L. Gargate, L. O. Silva, R. A. Fonseca, M. Hapgood, C. Norberg, T. Todd, and R. Stamper, Plasma Phys. Control. Fusion **50**, 124025 (2008).
[10] A. Knapp, H. Fulge, G. Herdrich, N. Ono, R. Wernitz, M. Auweter-Kurtz, H.-P. Röser, and S. Fasoulas, Open Plasma Phys. J. **5**, 11 (2012).
[11] J. K. Olthoff and K. E. Greenberg, J. Res. Natl. Inst. Stand. Technol. **100**, 327 (1995).
[12] Finite Elements Method Magnetics version 4.2, http://www.femm.info/, 2013.
[13] J. R. Creel, Master thesis, Baylor University, 2010.
[14] F. F. Chen, *Introduction to Plasma Physics and Controlled Fusion*, 2nd ed. (Plenum Press, New York, 1984).
[15] A. V. Phelps, J. Appl. Phys. **76**, 747 (1994).
[16] A. Douglass, V. Land, K. Qiao, L. Matthews, and T. Hyde, Phys. Plasmas **19**, 013707 (2012).
[17] V. N. Tsytovich, N. Sato, and G. E. Morfill, New J. Phys. **5**, 43 (2003).
[18] Y. Nakamura and M. Kurachi, J. Phys. Appl. Phys. **21**, 718 (1988).
[19] H. W. Kuhn, Nav. Res. Logist. Q. **2**, 83 (1955).
[20] P. S. Epstein, Phys. Rev. **23**, 710 (1924).
[21] B. Liu, J. Goree, V. Nosenko, and L. Boufendi, Phys. Plasmas 1994–Present **10**, 9 (2003).
[22] J. Carstensen, F. Haase, H. Jung, B. Tadsen, S. Groth, F. Greiner, and A. Piel, IEEE Trans. Plasma Sci. **41**, 764 (2013).
[23] V. E. Fortov, A. G. Khrapak, S. A. Khrapak, V. I. Molotkov, and O. F. Petrov, Phys.-Usp. **47**, 447 (2004).
[24] V. Land, L. S. Matthews, T. W. Hyde, and D. Bolser, Phys. Rev. E **81**, 056402 (2010).